



Promotion of Dense Shelf Water formation in the Ross Sea under the future trend of the Amundsen Sea Low

3 Zhaoru Zhang^{*1,2,3,4}, Heng Hu¹, Xiaoqiao Wang^{5,6}, Yuanjie Chen¹, Chunling Wang¹, and
4 Chuan Xie¹

¹ Key Laboratory of Polar Ecosystem and Climate Change, Ministry of Education; State Key Laboratory of Submarine Geoscience; School of Oceanography, Shanghai Jiao Tong University, Shanghai, China

⁸ ² Shanghai Key Laboratory of Polar Life and Environment Sciences, Shanghai Jiao Tong
⁹ University, Shanghai, China

10 ³ Shanghai Frontiers Science Center of Polar Science, Shanghai Jiao Tong University,
11 Shanghai, China

⁴ Key Laboratory for Polar Science, Polar Research Institute of China, Ministry of Natural Resources, Shanghai, China

14 ⁵ College of Meteorology and Oceanography, National University of Defense Technology,
15 Changsha, China

¹⁶ ⁶Key Laboratory of High Impact Weather (special), China Meteorological Administration,
¹⁷ Changsha, China

* Corresponding author : Zhaoru Zhang

Email: zrzhang@sjtu.edu.cn



18

19

ABSTRACT

20 The Amundsen Sea Low (ASL) is a key low-pressure system influencing climate variability
21 over West Antarctica. The Ross Sea is one of the major formation sites of Dense Shelf Water
22 (DSW), precursor of the global ocean bottom water mass — Antarctic Bottom Water. This
23 study uses CMIP6 multi-model ensemble means to project future changes in the ASL and the
24 associated wind variations over the Ross and Amundsen Seas by the mid- and late-21st century.
25 A high-resolution coupled ocean-sea ice-ice shelf model covering the Ross Sea and the
26 Amundsen Sea is employed to assess how these ASL-driven future wind changes affect DSW
27 formation in the Ross Sea. By applying ASL-induced wind perturbations to three key regions
28 that modulate the Ross Sea DSW characteristics, the respective contributions of regional wind-
29 driven ocean-ice coupling processes to the DSW formation are quantified. The results show
30 that the future deepening and southward shift of the ASL will enhance sea ice production in
31 the Ross Sea polynyas and reduce meltwater inflow from Amundsen Sea ice shelves, thereby
32 promoting DSW formation. Relative to present conditions, ASL-related wind changes over the
33 Ross Sea and adjacent Amundsen Sea are projected to increase DSW production by
34 approximately 8% by 2050 and 18% by 2100. These findings suggest that future ASL changes
35 could help counteract the diminishing trend of DSW in the Ross Sea and maintain the Southern
36 Ocean meridional overturning circulation.

37 **Key words:** Amundsen Sea Low, Dense Shelf Water, future variations, Ross Sea, Antarctica

38 **Article Highlights:**

39 ● The future changes of ASL will enhance sea ice production in the Ross Sea polynyas.



44

45



46 1 Introduction

47 The Antarctic bottom water (AABW) plays a significant role in the global climate system
48 by supplying the lower limb of the global meridional overturning circulation (Marshall and
49 Speer 2012) and transporting carbon from polar regions to the deep oceans (De Lavergne et
50 al., 2017; Sigman and Boyle, 2000). In the Pacific and Indian sectors of the Southern Ocean,
51 AABW is supplied by the Ross Sea Bottom Water (RSBW) (Rintoul, 2007; van Wijk and
52 Rintoul, 2014), which originates from the dense shelf water (DSW) primarily produced on the
53 western Ross Sea continental shelf. The high salinity is the result of dramatic sea ice production
54 in the coastal polynyas, including the Ross Ice Shelf polynya and the Terra Nova Bay polynya
55 (Nihashi and Ohshima, 2015; Tamura et al., 2016; Jendersie et al., 2018; Zhang et al., 2025).
56 Brine released during sea ice formation increases salinity of the surface waters, resulting in
57 ocean deep convection and ultimately the formation of DSW in the polynya regions (Fusco et
58 al., 2009).

59 In the past few decades, long-term hydrographic measurements in the Ross Sea have
60 revealed a marked decrease in the salinity of DSW (Jacobs et al., 2002; Jacobs and Giulivi,
61 2010; Jacobs et al., 2022). Meanwhile, ice shelves in the Amundsen Sea are experiencing
62 prominent increases in the basal melting over recent decades (Shepherd et al., 2018; Rignot et
63 al., 2019). Most of the freshening in the Ross Sea has resulted from an increasing volume of
64 ice shelf meltwater from the Amundsen Sea, which is transported westward to the Ross Sea by
65 the Antarctic coastal and slope currents (Jacobs et al., 2022). Recent studies found that the
66 DSW salinity rebounded after 2014 (Castagno et al., 2019), attributed to increased sea ice
67 formation in the Ross Sea resulting from reduced ice transport from the Amundsen Sea
68 (Silvano et al., 2020) or a reduction in freshwater transport from the Amundsen Sea (Guo et
69 al., 2021). From the short-term and long-term changes in DSW salinity, it can be found that



70 sea ice production in coastal polynyas in the Ross Sea and the freshwater input from the
71 Amundsen Sea are the two most important processes affecting the DSW formation in the Ross
72 Sea.

73 Winds over the Ross Sea and Amundsen Sea could affect both sea ice formation in the Ross
74 Sea polynyas and the transport of meltwater from the Amundsen Sea, and further affect the
75 DSW formation in the Ross Sea. Polynyas in the Ross Sea are formed and maintained by strong
76 offshore katabatic winds that are generated by the steep terrain along the coast (Bromwich and
77 Kurtz, 1984; Park et al., 2018). The offshore winds drive sea ice away from the coast,
78 increasing the open water area of the polynyas and leading to more ice production due to intense
79 oceanic heat loss to the atmosphere. Offshore winds can also be generated by large-, synoptic-
80 and meso-scale atmospheric circulations (Chenoli et al., 2015; Weber et al., 2016; X. Wang et
81 al., 2021; X. Wang et al., 2023; Zhang et al., 2024). The western Amundsen Sea is a key region
82 for the transport of meltwater and sea ice from the Amundsen Sea into the Ross Sea (Nakayama
83 et al., 2014; Xie et al., 2024; Xie et al., 2025). Easterly winds over the western Amundsen Sea
84 drive onshore Ekman transport and create a doming of the sea surface and deepening of the
85 pycnocline near the coast, thereby intensifying the westward coastal flows (Kim et al., 2016;
86 Dotto et al., 2018) that are crucial for the freshwater and ice transports. In the eastern
87 Amundsen Sea, zonal winds over the slope can modulate the on-shelf intrusion of warm
88 Circumpolar Deep Water (CDW), with stronger westerly winds leading to greater CDW
89 intrusion (Thoma et al., 2008; Wåhlin et al., 2013; Jenkins et al., 2018; Li et al., 2025). The
90 intruded CDW can be transported all the way to the ocean cavities beneath ice shelves and
91 cause basal melting (Paolo et al., 2015; Konrad et al., 2018). Nakayama et al. (2014) revealed
92 that a slight increase of the basal mass loss in the Amundsen Sea rapidly intensifies the basal
93 meltwater transport downstream into the Ross Sea.



94 The Amundsen Sea Low (ASL) is a climatological low-pressure system in the high-latitude
95 South Pacific sector of the Southern Ocean (Fig. 1), which covers the Ross Sea, the Amundsen
96 Sea, and the Bellingshausen Sea (Turner et al., 2013; Coggins and McDonald, 2015; Raphael
97 et al., 2016). It is strongly influenced by large-scale patterns of atmospheric variability, such
98 as the Southern Annular Mode (SAM) and El Niño Southern Oscillation (ENSO) (Clem et al.,
99 2017; Li et al., 2021). It has profound impacts on the atmospheric circulations over the Ross
100 Sea and Amundsen Sea regions, which will further impact the sea ice fields and oceanic
101 circulations (Holland et al., 2018; Raphael et al., 2019; Dotto et al., 2020; T. Wang et al., 2021;
102 S. Wang et al., 2023). By modulating the wind field over the Ross Sea region, a deeper and
103 more eastward ASL in November may result in a larger and more eastward-located Ross Ice
104 Shelf polynya in December (T. Wang et al., 2022). Guo et al. (2021) demonstrated that the
105 accelerated deepening of the ASL and the resulting southwestward extension of low pressure
106 induces eastward coastal current anomalies and reduces the freshwater input from the
107 Amundsen Sea to the Ross Sea, which is responsible for the subsequent increase of DSW
108 salinity in the western Ross Sea in recent years. Dotto et al. (2020) suggested that the fate of
109 the West Antarctic ice shelves is closely tied to the evolution of the ASL by establishing a link
110 between heat content on the Amundsen Sea shelf and local wind associated with the ASL. In
111 the future, the ASL is projected to deepen and migrate poleward significantly under high-level
112 warming scenarios based on the Coupled Model Intercomparison Project Phase 5 and 6
113 (CMIP5/6) models (Hosking et al., 2016; Gao et al., 2021), which will influence the
114 atmospheric circulations over the Ross Sea and the Amundsen Sea and can induce changes in
115 sea ice production, ice shelf basal melting and the transport of meltwater from the Amundsen
116 Sea, all of which will possibly affect the formation of DSW in the Ross Sea. Up until now, the
117 impacts of the future ASL changes on the DSW formation have not been revealed, which is the
118 objective of this study.

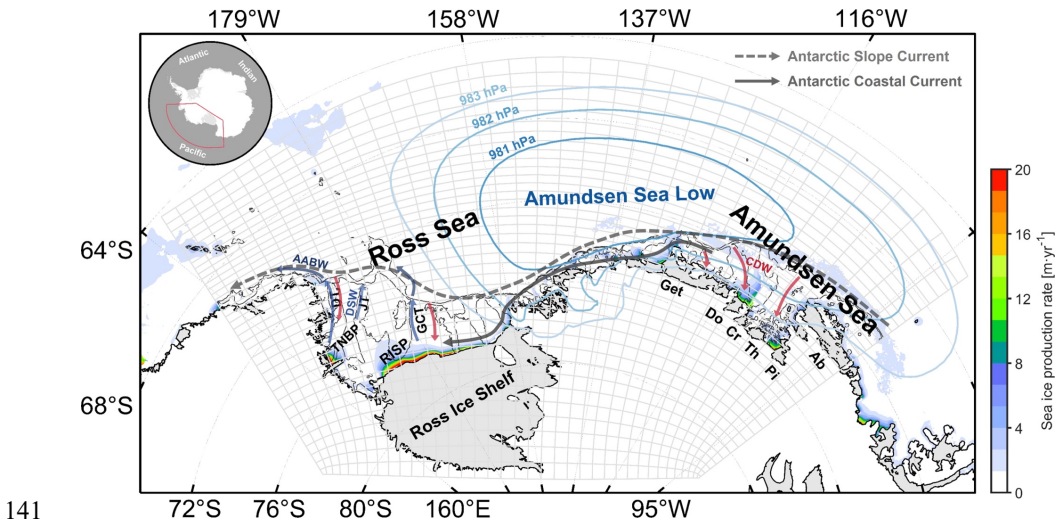


119 In this work, a high-resolution coupled ocean-sea ice-ice shelf model covering the Ross Sea
120 and Amundsen Sea was developed to investigate the effects of future wind changes related to
121 the ASL change on the DSW formation in the Ross Sea. Multi-model ensemble mean results
122 from CMIP6 were used to project the future changes of ASL properties, and the projected
123 changes in wind caused by the ASL variation were obtained based on the statistical relationship
124 between the two quantities over the historical period. Sensitivity experiments were conducted
125 by applying wind perturbations associated with ASL changes over the Ross Sea shelf, the
126 western Amundsen Sea, and the eastern Amundsen Sea shelf and slope region respectively.
127 Changes in DSW production in the Ross Sea in these experiments were quantified and the
128 physical mechanisms for these changes were revealed.

129 **2 Methodology**

130 **2.1 Numerical model**

131 The high-resolution ocean-sea ice-ice shelf model of the Ross Sea and Amundsen Sea
132 employed in this study, named the **Ross-Amundsen Sea Ice-Sea Model (RAISE; Zhang et al.,**
133 **2025)**, was developed based on the Regional Ocean Modeling System (ROMS). ROMS is a
134 free-surface, terrain-following coordinate, primitive equations ocean circulation model
135 developed for coastal ocean modeling studies (Haidvogel et al., 2008; Shchepetkin and
136 McWilliams, 2009). The model domain (Fig. 1) extends from roughly 85.6°S to 64.2°S and
137 from 143.0°E to 89.9°W, which covers the entire Ross Sea and the Amundsen Sea, including
138 the portion underneath the floating ice shelves. The model horizontal resolution varies from ~2
139 km in the coastal regions to ~6 km in the open ocean. The model includes 32 vertical levels
140 that are concentrated near the surface and the sea floor.



141
142 **Figure 1.** Domain and grid of the coupled ocean-sea ice-ice shelf model (RAISE) over the
143 Ross Sea and the Amundsen Sea. The inset shows the location of model domain in the Southern
144 Ocean. The isobars indicate the climatological condition of the Amundsen Sea Low (ASL).
145 The blue arrows indicate the movement of Dense Shelf Water (DSW) and Antarctic Bottom
146 Water (AABW), while the red arrows indicate the movement of Circumpolar Deep Water
147 (CDW). The color indicates the sea ice production rate. The Terra Nova Bay polynya (TNBP)
148 and Ross Ice Shelf polynya (RISP) are labeled. The gray areas indicate ice shelves. Local ice
149 shelves including the Abbot Ice Shelf (Ab), Pine Island Ice Shelf (Pi), Thwaites Ice Shelf (Th),
150 Crosson Ice Shelf (Cr), Dotson Ice Shelf (Do), and Getz Ice Shelf (Get) are labeled. The gray
151 lines indicate the 500-m and 1000-m isobaths.

152 The model bathymetry and ice shelf draft have been interpolated from BedMachine-
153 Antarctica-v2.0 (Morlighem et al., 2020), which has a spatial resolution of 500 m on the
154 Antarctic Polar Stereographic projection. Sea ice is simulated with a dynamic sea ice model
155 (Budgell 2005) coupled with the ROMS model. The ice dynamics are based on elastic-
156 viscous-plastic rheology (Hunke and Dukowicz 1997; Hunke 2001). The ice thermodynamics



157 are described by Mellor and Kantha (1989) and Häkkinen and Mellor (1992). In this model,
158 sea ice is represented by two layers and temperature gradients within the ice are allowed. A
159 snow layer is included, which acts as an insulating layer and changes the surface albedo. This
160 model also includes the mechanical and thermodynamic effects of ice shelves on the waters
161 beneath based on the three-equation parameterization (Holland and Jenkins, 1999; Dinniman
162 et al., 2011). The ice shelves in the model are static, and there is no mass variation of the ice
163 shelf or any iceberg calving parameterization. Vertical mixing of momentum and tracers are
164 computed using the K-profile parameterization (KPP) mixing scheme (Large et al., 1994).

165 Atmospheric forcings for this model come from the ERA5 reanalysis product (Hersbach et
166 al., 2020), which include wind speed, sea level pressure, humidity, air temperature, cloud cover
167 and precipitation. The atmospheric forcing fields use 3-hourly data for wind and air
168 temperature, and daily data for other variables. Initial conditions of temperature and salinity
169 are taken from the 10-km horizontal-resolution circum-Antarctic ocean-sea ice-ice shelf model
170 (Dinniman et al., 2015). The temperature, salinity, sea surface height, and depth-averaged
171 velocity for the open boundaries are derived from daily mean data produced by the Met Office
172 Global Seasonal forecasting system version 5 (GloSea5) (MacLachlan et al., 2015). Daily sea
173 ice concentration boundary conditions are obtained from the Advanced Microwave Scanning
174 Radiometer-Earth Observing System (AMSR-E) and Advanced Microwave Scanning
175 Radiometer 2 (AMSR2) dataset provided by the University of Bremen using the ARTIST sea
176 ice algorithm (Spreen et al., 2008). Tidal forcing is derived from the global tidal solution
177 TPXO9 (Egbert and Erofeeva 2002), including 15 major tidal constituents (K1, S2, M4, P1,
178 O1, Q1, S1, MS4, MN4, MF, 2N2, M2, K2, MM and N2), forced at the open boundaries
179 through sea surface height and barotropic currents.



180 In this study, a base simulation (named Present simulation) is obtained by initializing the
181 model from a 7-yr spin-up simulation from 1998 to 2004 and integrating it from 2005 to 2014.
182 Extensive validation of the base simulation has been presented in Zhang et al. (2025), Zhang
183 et al. (2024) and Xie et al. (2024), confirming the model's strong capability in reproducing key
184 physical processes associated with DSW production and transport in the Ross Sea and
185 Amundsen Sea. The simulations successfully capture the sea-ice and DSW production rates
186 within the Ross Sea polynyas, the DSW export rates at the trough exits, the temporal evolution
187 of DSW salinity and density as well as the ice shelf melting rates in the Amundsen Sea. The
188 simulated interannual variability of DSW salinity near the Ross Ice Shelf polynya is
189 significantly correlated with that from 17-year on-site observational data ($R=0.66$, p -
190 value=0.004), and the simulated variability of DSW neutral density at a major DSW export
191 outlet in the Ross Sea is highly correlated with that from 4-year mooring measurements
192 ($R=0.75$, p -value<0.001) (Zhang et al., 2025).

193 **2.2 Sensitivity experiments**

194 **2.2.1 Deriving the relation between long-term variability of the ASL and wind**

195 Following Hosking et al. (2013), three indices are used to describe the ASL depth and
196 positions, including the actual central pressure (ACP), longitude (LON) and latitude (LAT).
197 The ASL center is defined as the location with minimum MSLP value over the ASL sector
198 (170–298°E, 80–60°S) following Hosking et al. (2016). In this study, annual ASL indices are
199 defined by the annual mean sea level pressure (MSLP) from ERA5 for the present period or
200 CMIP6 for the future periods.

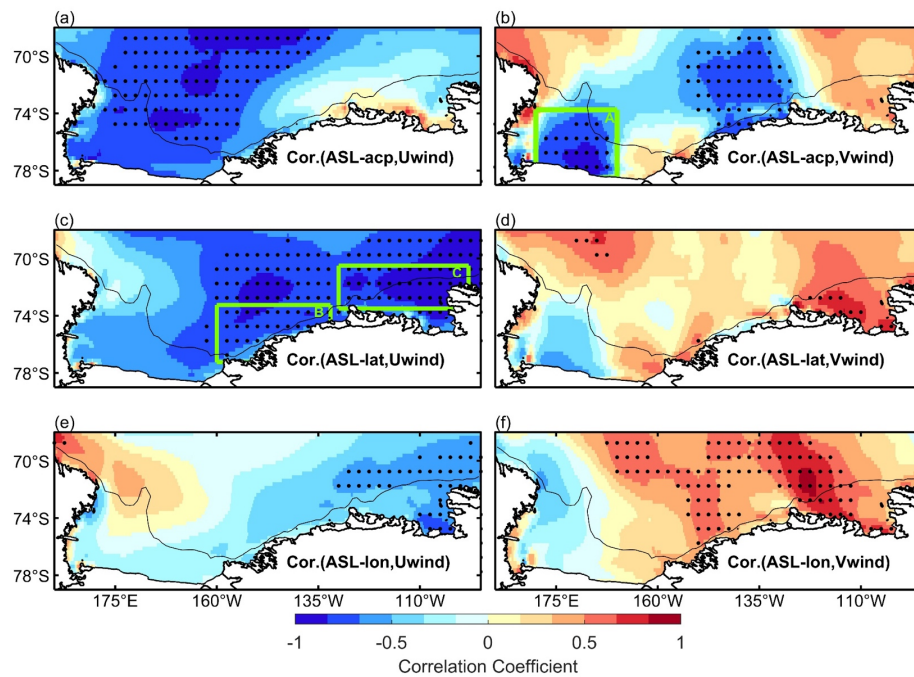
201 To describe the relationship between variations of ASL indices and wind speed over the
202 study areas on interdecadal timescales (~10 years), we performed a correlation analysis
203 between the anomalies of ASL indices and each wind component for the period 1959–2021



204 using the ERA5 product (Fig. 2). The anomaly time series are smoothed with a 10-year running
205 mean to extract the interdecadal variability following Henley et al. (2015), and effective
206 degrees of freedom are used to test the significance of correlation (Bretherton et al., 1999). For
207 the sensitivity experiments described in the next section, wind changes associated with the
208 future variations of ASL indices are added to the atmospheric forcings over three crucial
209 regions, which exhibit significant correlations between the ASL indices and wind as illustrated
210 in Fig. 2. The first region is the central Ross Sea shelf, which includes one important formation
211 site for the DSW formation — the Ross Ice Shelf polynya (166–194°E and 76.5–78.5°S). A
212 significant negative correlation exists between the variations of meridional wind component
213 and ASL-ACP (Fig. 2b). Therefore, in the sensitivity experiment we would consider the
214 perturbations of meridional wind component caused by the ASL-ACP variation in this area.
215 The second region is the western Amundsen Sea (referred to as WAS and denoted as region B
216 in Fig. 2e, spanning 200–228°E and 73.25–77.25°S), which is the key region for westward
217 transport of ice shelf meltwater from the Amundsen Sea to the Ross Sea (Silvano et al., 2020).
218 The third region is the eastern Amundsen Sea shelf and slope region (referred to as EASS and
219 denoted as region C in Fig. 2e, spanning 230–262°E and 70.5–73.5°S), where zonal winds can
220 significantly affect the on-shelf intrusion of CDW and thus melting of major ice shelves in the
221 Amundsen Sea (Jenkins et al., 2018; Silvano et al., 2022). In both the second and third regions,
222 significant negative correlations exist between the ASL-LAT and the zonal wind speed (Fig.
223 2e), while the correlations between ASL indices and the meridional wind are not significant
224 (Figs. 2b,d,f,h). As such, in the sensitivity experiments we apply perturbations of zonal winds
225 associated with the ASL-LAT variability to the atmospheric forcings over these two regions.
226 ASL is also shown to modulate air temperature and moisture advection via control of winds
227 over the West Antarctica (Nicolas and Bromwich, 2011; Bromwich et al., 2011) and the Ross



228 Sea (Cohen et al., 2013). However, our analysis reveals no significant correlations between
229 variations in air temperature or humidity and ASL properties across the three regions.



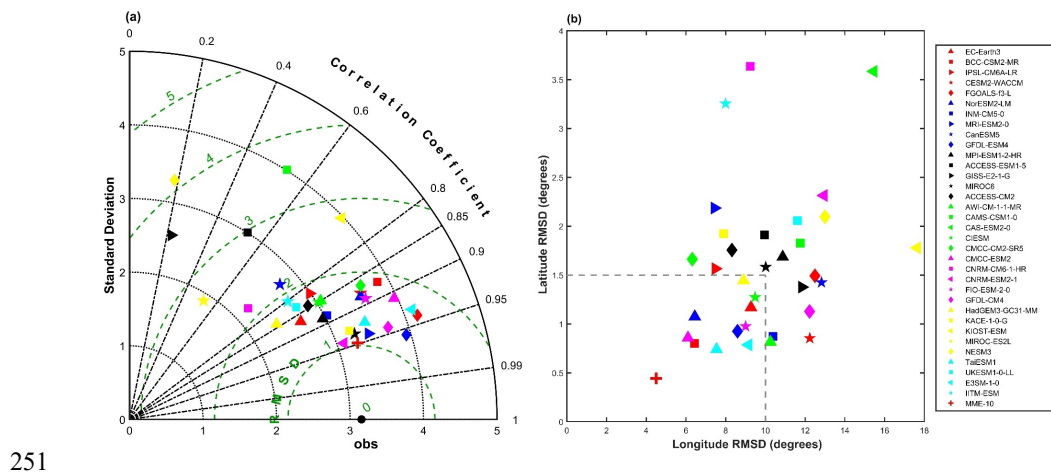
230

231 **Figure 2.** (a, c, e) Spatial distributions of correlation coefficients between the interdecadal
232 variability of zonal wind anomalies and (a) ASL-ACP, (c) ASL-LAT and (e) ASL-LON
233 anomalies. (b, d, f) Spatial distributions of correlation coefficients between the interdecadal
234 variability of meridional wind anomalies and (b) ASL-ACP, (d) ASL-LAT and (f) ASL-LON
235 anomalies in the Ross Sea and Amundsen Sea. All anomaly time series are smoothed with a
236 10-year running mean from 1959 to 2021. The green boxes show the three key regions where
237 wind perturbations associated with the ASL changes are applied in the sensitivity experiments.
238 Dots represent correlations significant at the 95% confidence level. The thin black line
239 indicates the 1000-m isobath.

240 **2.2.2 The projection of future ASL changes based on CMIP6 models**



241 Gao et al. (2021) evaluated historical simulations of climatological characteristics of ASL
 242 in CMIP5 and CMIP6 against the ERA5 reanalysis product. Both the spatial distribution and
 243 annual cycle of ASL are improved in CMIP6 multi-model ensemble mean compared to CMIP5,
 244 and the dispersion of ASL-ACP, ASL-LAT, and ASL-LON simulated by CMIP6 models are
 245 much smaller than those in CMIP5. Here, we used the ERA5 product to validate the
 246 representation of ASL-ACP (Fig. 3a), LAT and LON (Fig. 3b) in the historical simulations
 247 (1850–2014) of 34 CMIP6 models during 1959–2014. 10 models with the lowest root mean
 248 square deviations (RMSD) in the ASL-ACP, LAT and LON were selected, which are EC-
 249 Earth3, BCC-CSM2-MR, NorESM2-LM, CMCC-ESM2, GFDL-ESM4, CIESM, FIO-ESM-
 250 2-0, HadGEM3-GC31-MM, E3SM-1-0 and TaiESM1 (Figs. 3a,b).



251

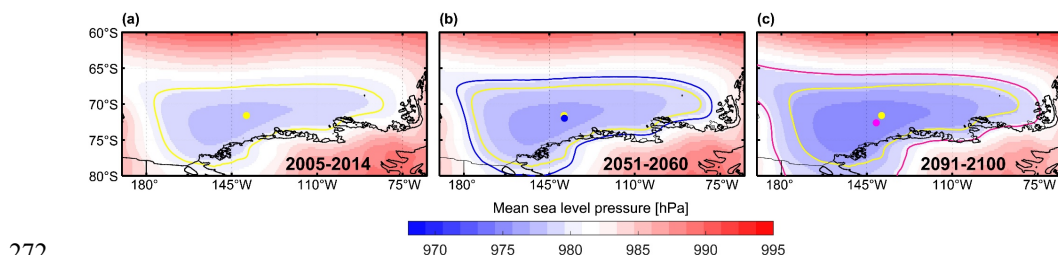
252 **Figure 3.** (a) Taylor diagram of the actual central pressure of the ASL (ACP) in CMIP6 models
 253 against the ERA5 product during 1959–2014. (b) Scatterplot of the root mean square deviations
 254 (RMSD) for 34 CMIP6 models relative to ERA5 for longitude (LON) and latitude (LAT) of
 255 the ASL over the period 1959–2014. 10 models with the lowest RMSD values in both the ASL
 256 LAT and LON (those that lie within the dashed lines) are selected. Red cross denotes the value
 257 of the 10-model-mean (CMIP6-MME10) in this study.



258 Using the ensemble mean results of the 10 models (named as CMIP6-MME10) selected
 259 above, we examined how the ASL indices will change under a high-emission scenario —
 260 SSP585 in the future. The projected ASL features were examined for two 10-year periods
 261 respectively in the middle (2051–2060) and end (2091–2100) of the twenty-first century. The
 262 CMIP6-MME10 MSLP for the present period (2005–2014), 2051–2060 and 2091–2100 are
 263 shown in Figs. 4a, 4b, and 4c, respectively. The differences in the ASL indices in the future
 264 periods compared to the present period are listed in Table 1. The changes in ACP are
 265 significant, which are 1.27 hPa and 2.87 hPa deeper in 2051–2060 and 2091–2100 than the
 266 present period, respectively. The ASL will move southward by 0.38° in 2051–2060 and 1.01°
 267 in 2091–2100, respectively, while no significant changes in the ASL longitude are found.
 268 **Table 1.** Projected changes of ASL central pressure (ACP), latitude (LAT) and longitude
 269 (LON) from CMIP6-MME10 under the SSP585 scenario relative to the present period (2005–
 270 2014). Stars denote changes significant at the 95% confidence level.

	2005–2014	2051–2060	2091–2100
ACP (hPa)	976.95	975.68*	974.08*
LAT (°S)	71.60	71.98	72.61*
LON (°E)	221.04	221.20	218.86

271



272

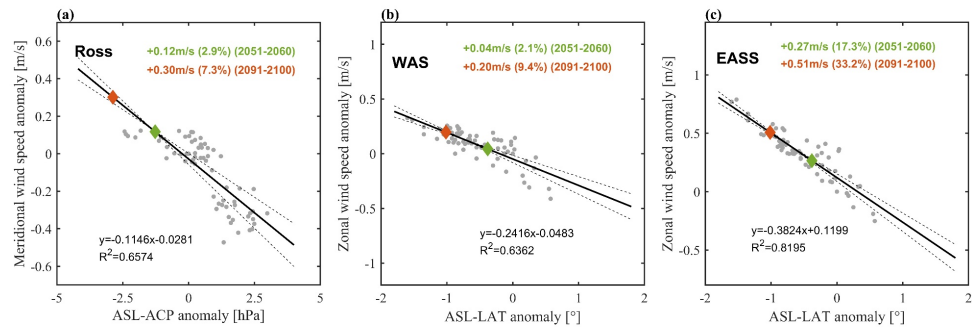


273 **Figure 4.** Mean sea level pressure from CMIP6-MME10 during (a) 2005–2014, (b) 2051–2060
274 and (c) 2091–2100. The yellow, blue and magenta contour lines and dots denote the 980-hPa
275 isobar and the central location of the ASL during 2005–2014, 2051–2060 and 2091–2100,
276 respectively.

277 **2.2.3 Wind perturbation sensitivity experiments**

278 Linear relations between the anomalies of wind speed and ASL indices are derived for each
279 of the three regions using the ERA5 reanalysis from 1959 to 2021, as shown in Fig. 5. Then,
280 based on these relations and projected changes in the depth and position of ASL from CMIP6-
281 MME10, changes in wind associated with the ASL index variation for each of the three regions
282 relative to the present period are derived. Over the Ross Sea shelf, a deeper ASL results in an
283 increase in southerly wind by 2.9% for 2051–2060 and 7.3% for 2091–2100 (Fig. 5a). Over
284 the WAS, the average easterly wind is projected to decrease by 2.1% for 2051–2060 and 9.4%
285 for 2091–2100 compared to present period under the southward shift of the ASL (Fig. 5b).
286 Over the EASS, the average easterly wind will decrease by 17.3% for 2051–2060 and 33.2%
287 for 2091–2100 as the ASL shifts southward (Fig. 5c).

288



289



290 **Figure 5.** Linear regression between the anomalies of annual wind speed and ASL indices in
291 1959–2021 over (a) the Ross Sea shelf (Ross), (b) the western Amundsen Sea (WAS) and (c)
292 the eastern Amundsen slope and shelf (EASS). The coefficient of determination (R^2) and
293 regression equation are shown in each panel. The gray dotted line in each panel denotes the
294 uncertainty range of the regression slope at the 95% confidence interval. The green and orange
295 diamonds on the dashed lines represent the projections of ASL indices based on CMIP6-
296 MME10 for 2051–2060 and 2091–2100, respectively. The green and orange numbers in each
297 panel are the projected changes of wind speed derived from the linear relationship for the
298 periods 2051–2060 and 2091–2100, respectively. The percent changes in the wind speed
299 relative to the values in the present period are shown in brackets in each panel.

300 Numerical sensitivity experiments were conducted by applying the projected
301 wind changes associated with the ASL variations to the atmospheric forcing fields for the
302 Present simulation over each of the three key regions. In addition, we also applied wind
303 perturbations over these three regions simultaneously to study the overall changes in the DSW
304 formation (the experiments are named “Total”). Configurations of these experiments are
305 summarized in Table 2. Modifications were made to the present wind field via scaling each
306 wind component by a constant factor estimated from Fig. 5. Except for wind, other atmospheric
307 forcing variables and boundary conditions are the same as in the Present simulation. In the
308 model we also set dyes for meltwater originating from basal melting of ice shelves in the
309 Amundsen Sea, to trace the meltwater transport into the Ross Sea. The content of the dye
310 release is proportional to the melting rate of the ice shelf at each grid following Xie et al.
311 (2024).

312

313



314 **Table 2.** Summary of the configurations for the Present simulation and sensitivity experiments.

Experiment	Region for applying the wind field perturbation	Simulation period	Wind perturbation related to the ASL change
Present	/	2005–2014	/
Ross-2050F	Ross Sea shelf	2051–2060	Southerly $\times(1+2.9\%)$
Ross-2100F		2091–2100	Southerly $\times(1+7.3\%)$
WAS-2050F	Western Amundsen Sea	2051–2060	Easterly $\times(1-2.1\%)$
WAS-2100F		2091–2100	Easterly $\times(1-9.4\%)$
EASS-2050F	Eastern Amundsen Sea shelf	2051–2060	Easterly $\times(1-17.3\%)$
EASS-2100F	and slope	2091–2100	Easterly $\times(1-33.2\%)$
Total-2050F	Ross Sea shelf, Western	2051–2060	All of the wind
Total-2100F	Amundsen Sea and Eastern Amundsen Sea shelf and slope	2091–2100	perturbations above

315 All simulations start from the end of the 5-yr spin-up simulation for the base simulation
316 mentioned in Section 2 and are integrated for 5 years. Unless explicitly stated, all results
317 analyzed below are from the last year of each simulation, which represent the most stable ocean
318 state.

319 **3 Results**



320 **3.1 Changes in DSW formation caused by ASL-induced wind changes over the Ross Sea**

321 **continental shelf**

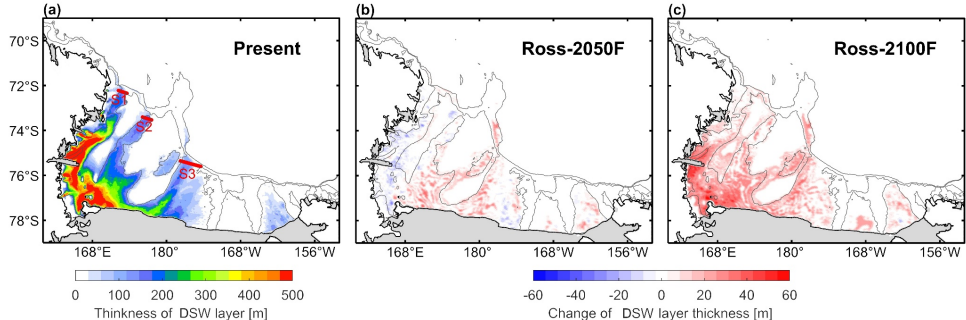
322 As shown in Fig. 6a, the majority of DSW (defined as neutral density $\gamma^n > 28.27 \text{ kg m}^{-3}$)
323 in the Ross Sea is formed within the Terra Nova Bay polynya and the western section of the
324 Ross Ice Shelf polynya. For the Ross-2050F and Ross-2100F simulations, under the enhanced
325 southerly winds, which are offshore winds for the Ross Ice Shelf polynya, sea ice production
326 in the Ross Sea during the ice freezing season (March–October) increased by $19.8 \text{ km}^3 \text{ yr}^{-1}$ and
327 $51.2 \text{ km}^3 \text{ yr}^{-1}$, respectively. The changes in sea ice production directly affect the DSW
328 formation through salt release. Differences between the DSW layer thicknesses in Ross-
329 2050F/Ross-2100F and the Present simulation over the Ross Sea shelf are shown in Figs. 6b,c.
330 Substantial increases in the DSW layer thicknesses are observed over the majority of the
331 western Ross Sea in Ross-2050F/Ross-2100F, with the most pronounced increases present in
332 the western Ross Ice Shelf polynya and the Terra Nova Bay polynya. The DSW volume over
333 the Ross Sea shelf in the Ross-2050F and Ross-2100F simulations are greater than that at
334 present by 1.6% and 8.8%, respectively (Table 3). We also selected three transects (S1, S2 and
335 S3 in Fig. 6a) across three troughs — the Drygalski Trough (DT), the Joides Trough (JT) and
336 the Glomar Challenger Trough (GCT) that are major passages for the DSW outflows, and
337 calculated the total DSW exports toward the slope through these transects. The DSW exports
338 in Ross-2050F show a slight increase (3.4%) compared to the Present simulation and a notable
339 increase (8.5%) in Ross-2100F, rising from 1.18 Sv in the Present simulation to 1.22 Sv and
340 1.28 Sv, respectively. Increases in DSW exports in Ross-2100F are primarily concentrated in
341 GCT and JT, contributing 70% and 20% of the total increase, respectively.

342 **Table 3.** Mean DSW volume on the Ross Sea shelf in different simulations. The numbers in
343 brackets show the changes as proportions of the DSW volume relative to the present.



Simulation	Present	Ross-2050F	Ross-2100F	WAS-2050F	WAS-2100F
DSW					
volume	4.34	4.41	4.72	4.43	4.62
(10 ⁴ km ³)					
(+1.6%)	(+8.8%)	(+2.1%)	(+6.5%)		
Simulation	EASS-2050F	EASS-2100F	Total-2050F	Total-2100F	
DSW					
volume	4.54	4.57	4.66	5.07	
(10 ⁴ km ³)					
(+4.6%)	(+5.3%)	(+7.4%)	(+16.8%)		

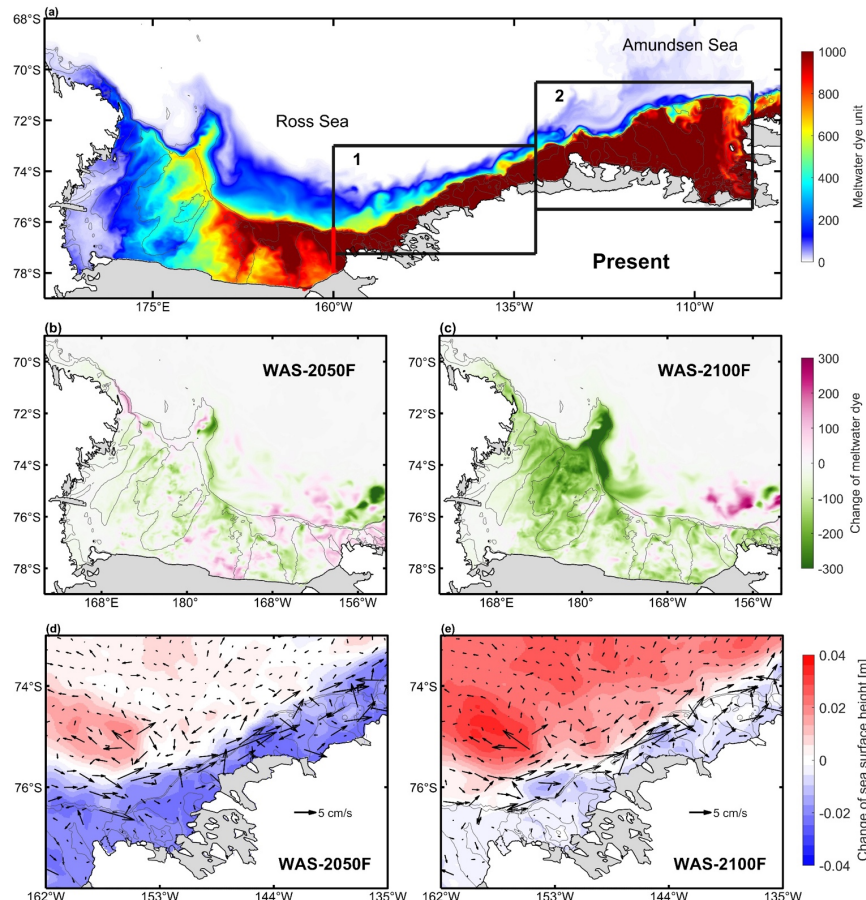
344



345

346 **Figure 6.** (a) Spatial distributions of the DSW layer thickness in the Ross Sea for the Present
 347 simulation. Changes in DSW layer thicknesses for (b) Ross-2050F and (c) Ross-2100F relative
 348 to the Present simulation. The red lines in (a) indicate the S1, S2 and S3 transects, and the gray
 349 lines indicate the 500-m and 1000-m isobaths.

350 **3.2 Changes in ice shelf meltwater transport in the western Amundsen Sea and the**
 351 **impacts on DSW production**



352

353 **Figure 7.** (a) Spatial distributions of meltwater dye unit released from the Amundsen Sea ice
354 shelves in the last year of the Present simulation. Changes in the meltwater dye unit over the
355 Ross Sea for the (b) WAS-2050F, (c) WAS-2100F simulations relative to the Present
356 simulation. Changes in sea surface height (SSH) from the (d) WAS-2050F and (e) WAS-2100F
357 simulations relative to the Present simulation, with changes in barotropic currents
358 superimposed. Black Box 1 in (a) indicates the region plotted for (d) and (e). Black Box 2 in
359 (a) indicates the region plotted for Figs. 8c and 8d. The red line in (a) represents the gate used
360 to estimate the sea ice import from the Amundsen Sea into the Ross Sea. Isobaths of 500-m
361 and 1000-m are shown by the black thin lines.



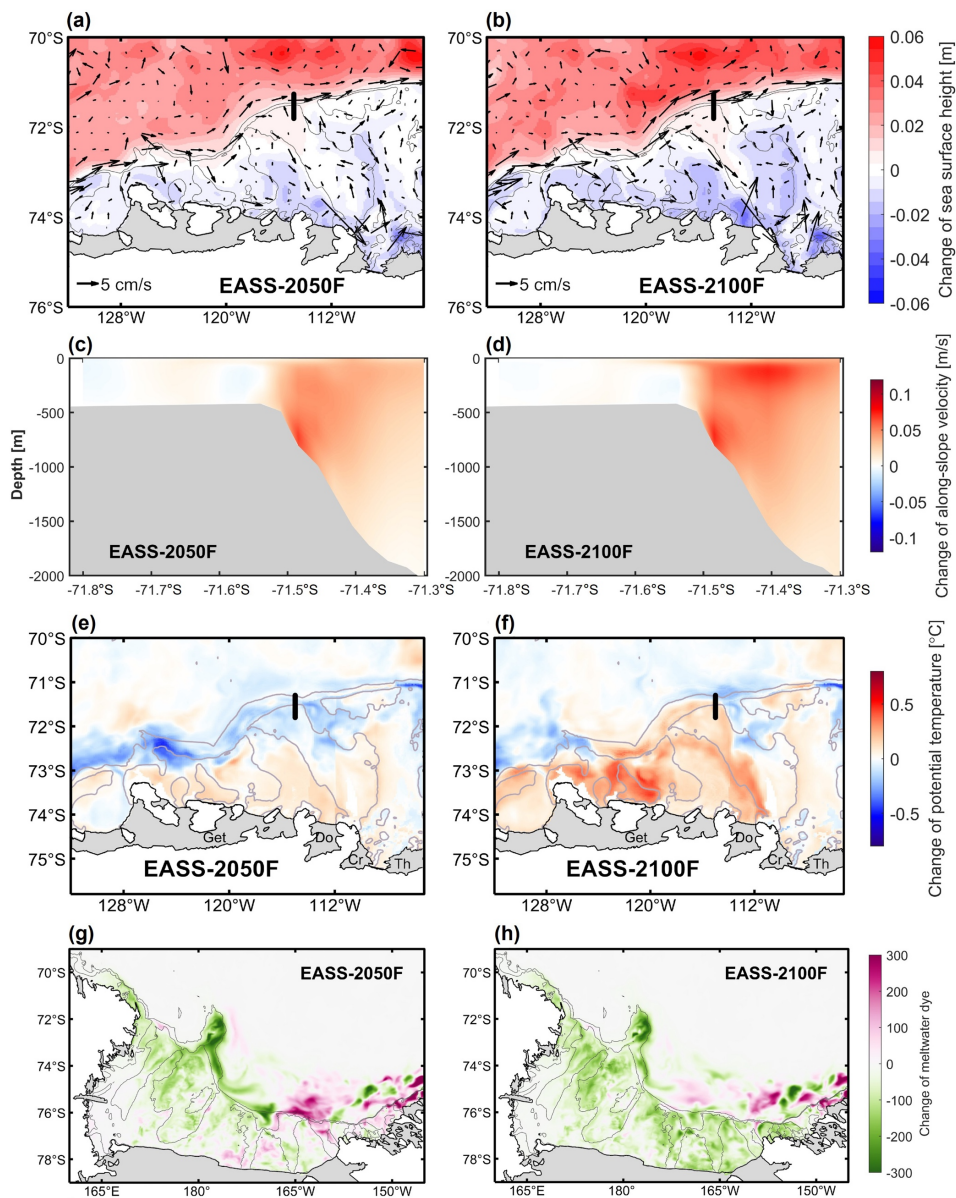
362 The dyes for tracing meltwater from the Amundsen Sea ice shelves clearly show westward
363 spreading in the Present simulation (Fig. 7a). For all simulations, meltwater is transported to
364 the Ross Sea shelf within 3 years after the dyes are released. In the future, the southward shift
365 of the ASL lead to a weakening of the easterly winds over the WAS (Fig. 5c and Table 2). This
366 results in a decrease in the amount of meltwater dyes entering the Ross Sea (Figs. 7b,c)
367 compared to the Present simulation, by 4.2% and 18.1% in WAS-2050F and WAS-2100F,
368 respectively. The reason for the decreased transport is that the weakened easterly winds
369 decreases the southward Ekman transport, reducing the cross-shelf sea surface height (SSH)
370 gradient and the westward barotropic coastal currents (Figs. 7d,e). As fresh meltwater from the
371 Amundsen Sea partially offsets the salt flux by sea ice formation in the Ross Sea polynyas and
372 inhibits the DSW formation (Silvano et al., 2018; Xie et al., 2025), the reduced meltwater
373 transport to the Ross Sea results in an increase of the mean DSW volume in the Ross Sea by
374 2.1% in WAS-2050F and 6.5% in WAS-2100F (Table 3). The DSW transports toward the slope
375 across the three transects in troughs increase by 2.5% and 10.2% in WAS-2050F and WAS-
376 2100F, respectively.

377 **3.3 Changes in CDW intrusion and ice shelf melting in the eastern Amundsen Sea and
378 impacts on the DSW production**

379 In the future, the southward shift of ASL will lead to a weakening of easterly winds over
380 the eastern Amundsen Sea shelf and slope (Fig. 5d). In EASS-2050F and EASS-2100F, the
381 easterly wind anomalies over the slope of the Amundsen Sea will enhance the eastward
382 barotropic currents (Figs. 8a,b), intensifying the eastward undercurrents in this area (Figs. 8c,d)
383 that would enhance the CDW intrusion based on previous studies (Wåhlin et al., 2013; Dotto
384 et al., 2020; Li et al., 2025). The potential temperature at 450 m in the CDW core layer on the



385 Amundsen Sea shelf shows a significant increase, indicating stronger CDW intrusion (Figs.
386 8e,f).



387

388 **Figure 8.** Changes in sea surface height (SSH) in the (a) EASS-2050F and (b) EASS-2100F
389 simulations relative to the Present simulation, with changes in barotropic currents



390 superimposed. (c, d) Vertical sections (see the section locations indicated as black lines in a
391 and b) of along-slope velocity changes (m s^{-1}) in the (c) EASS-2050F and (d) EASS-2100F
392 simulations relative to the Present simulation. The positive value denotes eastward velocity. (e,
393 f) Changes of potential temperature ($^{\circ}\text{C}$) at 450 m in the Amundsen Sea in the (e) EASS-2050F
394 and (f) EASS-2100F simulations. (g,h) Changes in meltwater dye units over the Ross Sea for
395 the (g) EASS-2050F and (h) EASS-2100F simulations relative to the Present simulation.
396 Isobaths of 500-m and 1000-m are shown by the gray thin lines.

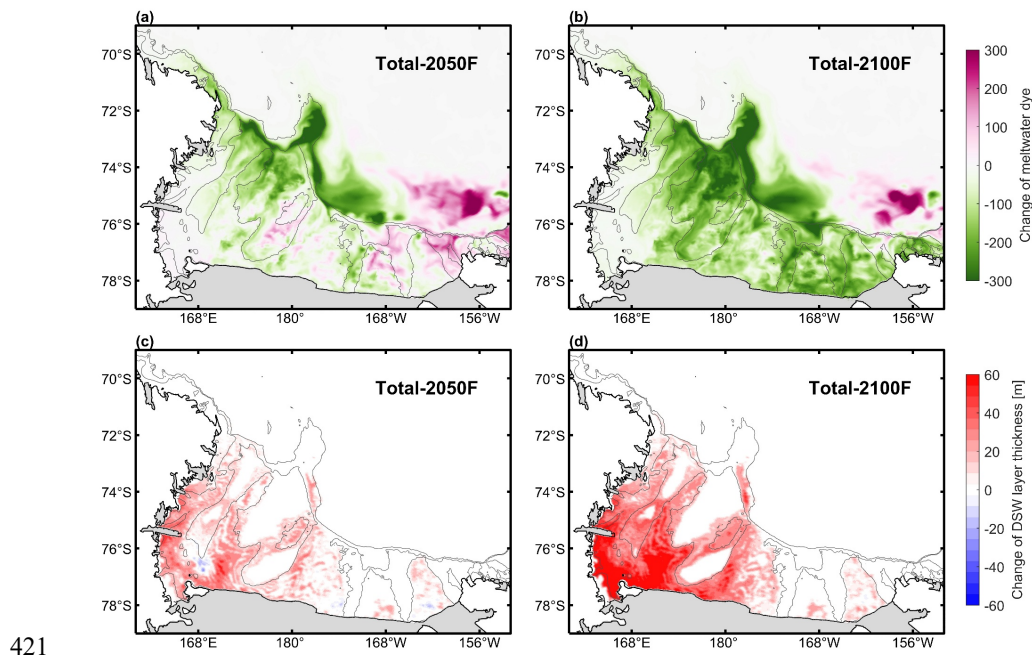
397 Heat content of the CDW layer on the Amundsen Sea shelf (230–260°E, south of 73°S) is
398 calculated from the temperature above the in-situ freezing point below 350 m over the
399 Amundsen Sea (Jacobs et al., 2011; Nakayama et al., 2013), based on the equation used in
400 Dotto et al. (2020). In EASS-2050F and EASS-2100F, the heat contents of the CDW layer on
401 the Amundsen Sea shelf increase by 45 and 109 GJ, respectively, compared to the Present
402 experiment. The enhanced ocean heat delivery by CDW over the Amundsen Sea resulted in
403 higher basal melt rates of the ice shelves, which increase by 25 and 44 Gt yr^{-1} for the total
404 Amundsen Sea ice shelves in EASS-2050F and EASS-2100F relative to the Present simulation,
405 respectively.

406 Despite increases in the Amundsen Sea ice shelf melting rates in EASS-2050F and EASS-
407 2100F, a reduction in meltwater reaching the Ross Sea shelf is found (Figs. 8g,h). Similar to
408 the WAS experiments, through Ekman transports, weakened easterly winds drive reduced sea
409 level near the coast, reducing the onshore SSH gradient and finally inducing anomalous
410 eastward barotropic flows (Figs. 8a,b). Compared with the WAS simulations, changes in SSH
411 and barotropic currents are more significant in EASS due to greater changes in winds. This
412 further reduces the barotropic westward transport of meltwater from the eastern Amundsen Sea.
413 The amount of meltwater dyes on the Ross Sea shelf decreases by 7.6% and 12.7% in EASS-



414 2050F and EASS-2100F, respectively. As a result of the reduced freshwater input to the Ross
415 Sea and increased salinity in this region, the DSW volume over the Ross Sea shelf increases
416 by 4.6% in EASS-2050F and 5.3% in EASS-2100F (Table 3). Such changes are not as
417 significant as those in the Ross and WAS experiments, possible because of the large distance
418 from the eastern Amundsen Sea to the Ross Sea.

419 **3.4 Total changes in DSW formation caused by ASL-induced process changes over the**
420 **three regions**



421
422 **Figure 9.** Changes in meltwater dye units in the Ross Sea for the (a) Total-2050F and (b) Total-
423 2100F simulations relative to the Present simulation. Changes in the DSW layer thicknesses
424 for (c) Total-2050F and (d) Total-2100F relative to the Present simulation. Isobaths of 500-m
425 and 1000-m are shown by the black thin line.



426 Due to the complex interactions among processes in the Ross Sea and Amundsen Sea
427 regions, additional experiments are conducted (named Total-2050F and Total-2100F, Table 2)
428 in which wind perturbations associated with the future changes of ASL are applied
429 simultaneously over of the three regions. In Total-2050F and Total-2100F, the amounts of
430 meltwater dye entering the Ross Sea shelf decrease by 10.8% and 28.0%, respectively (Figs.
431 9a,b). Meanwhile, the sea ice production over the Ross Sea shelf in the two simulations
432 increases by 1.4% and 8.4%, respectively. The reduction in meltwater input and the increase
433 in sea ice production together promote the DSW formation in the Ross Sea, as significant
434 thickening of the DSW layer in the western Ross Sea is observed in Total-2050F and Total-
435 2100F (Figs. 9c,d). The DSW volume on the Ross Sea shelf increases by 7.4% in Total-2050F
436 and 16.8% in Total-2100F (Table 3). The transport of DSW toward the slope across the three
437 transects in the troughs increases by 7.6% and 10.2% in Total-2050F and Total-2100F,
438 respectively. Among the three troughs, the outflow flux in the GCT exhibited the most
439 pronounced increase, contributing 56% and 75% to the total increase in DSW outflow fluxes
440 across the three transects in 2050 and 2100, respectively.

441 **4 Discussion**

442 For the western Amundsen Sea, besides the impact on meltwater transport, Silvano et al.
443 (2020) demonstrated that enhanced easterly winds over this area can increase the sea ice import
444 from the Amundsen Sea into the Ross Sea, increasing sea ice concentration on the Ross Sea
445 shelf and reducing sea ice production and ocean salinity. We found that in WAS-2100F, under
446 the weakened easterly winds, the sea ice import from the Amundsen Sea into the Ross Sea
447 decreases by 15.5% relative to the present period. However, sea ice production over the Ross
448 Sea shelf only shows a slight increase of 1.1% relative to the Present simulation. These findings
449 suggest that the impact of sea ice import from the Amundsen Sea on the Ross Sea DSW



450 formation associated with the ASL change is minor, compared to the impact of meltwater
451 transport.

452 All simulation results presented in this study focus on annual mean or annual cumulative
453 (e.g. sea ice production) parameters, and do not emphasize seasonality. As sea ice production
454 in the polynyas primarily occurs in March–October, we examined the relationship between
455 ASL indices and wind speed over the Ross Sea shelf during this ice freezing season, and also
456 found a significant negative correlation between the ASL-ACP and the meridional wind
457 component ($R=-0.72$). Using estimates of the ASL-ACP from the CMIP6-MME10 result, we
458 found that ASL-induced changes in wind speed during the ice freezing season are comparable
459 to that of the annual mean and does not significantly affect our results.

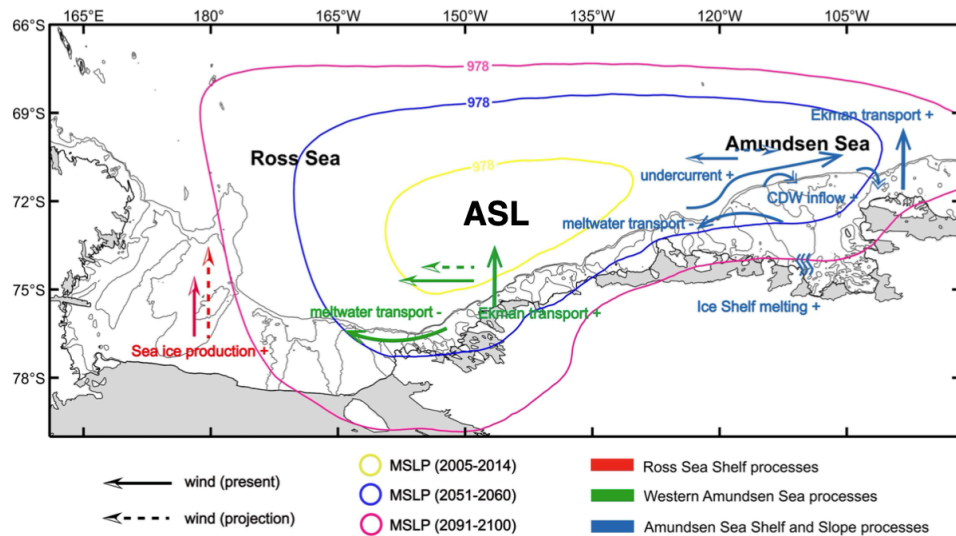
460 In the Total-2100F simulation, the ASL-induced atmospheric changes over the three study
461 regions could result in a combined increase of 16.8% in 2100. Dinniman et al. (2018) used
462 atmosphere forcing fields from the CMIP3 A1B emissions scenario to drive a coupled ocean-
463 sea ice-ice shelf model for the Ross Sea, and found that the DSW volume will decrease by
464 18.6%. Using the ensemble-mean atmospheric fields from 21 CMIP6 models under the SSP585
465 scenario to drive the coupled ocean-sea ice-ice shelf model employed in this study, Xie et al.
466 (2025) showed that the DSW volume in the Ross Sea will decrease by 51% in 2100, as a result
467 of increased freshwater input from the Amundsen Sea and decrease in sea ice production in the
468 Ross Sea polynyas. In such context, the increase in DSW production caused by ASL (16.8%)
469 until the end of this century is important for reducing the current decreasing trend of DSW
470 volume, and for maintaining the AABW production in the Southern Ocean Pacific and Indian
471 sectors.

472 **5 Conclusions**



473 Climate variability over the West Antarctica region is largely driven by the Amundsen Sea
474 Low and associated wind fields. This study focuses on the impacts of future ASL changes on
475 the formation of DSW — the precursor for AABW in the Ross Sea, Antarctica. In this work,
476 ten models are selected from CMIP6 based on their good performance in simulating the ASL
477 indices, and the ensemble mean of their future projections under the SSP585 scenario are used
478 to derive the ASL changes by the middle and end of the 21st century, as well as the associated
479 wind changes. It is found that the deepening and southward shift of the ASL in the future drive
480 significant anomalous southerly winds over the Ross Sea and westerly winds over the western
481 and eastern Amundsen seas. To quantify how ASL-driven, regionally distinct ocean-sea ice-
482 ice-shelf coupling processes influence DSW formation in the Ross Sea, we conduct sensitivity
483 experiments in which wind anomalies associated with future ASL changes are imposed on each
484 of the three regions.

485 Results from the sensitivity experiments are summarized in Fig. 10. The future deepening
486 of ASL will strengthen southerly winds over the Ross Sea shelf, promoting sea ice production
487 and DSW formation in the Ross Sea polynyas. Meanwhile, in the Amundsen Sea, the future
488 southward shift of ASL will result in reduced easterly winds, decreasing the transport of ice
489 shelf meltwater from the Amundsen Sea to the Ross Sea and thereby promoting the DSW
490 formation. Although the ASL-induced weakening of easterly winds can enhance the melting
491 of Amundsen Sea ice shelves and promote the meltwater release, the significant weakening of
492 barotropic transport of meltwater from the Amundsen Sea to the Ross Sea caused by the wind
493 changes finally leads to more DSW formation in the Ross Sea. These findings highlight the
494 crucial contributions of the future ASL changes to the production of DSW, indicating that the
495 ASL variations can play an inhibitory role in the future diminishing trend of DSW in the Ross
496 Sea, which helps to maintain the AABW production and characteristics in the Pacific and
497 Indian sectors as well as the Southern Ocean meridional overturning circulation.



498

499 **Figure 10.** Schematic illustrating the physical mechanisms driving enhanced DSW formation
500 in the Ross Sea caused by future ASL changes. Symbols in red, yellow and blue indicate
501 processes in the Ross Sea, western Amundsen Sea and eastern Amundsen Sea shelf and slope
502 region, respectively. The plus symbol indicates enhancement in the corresponding process,
503 while the minus symbol indicates weakening. Isobaths of 500-m and 1000-m are shown by the
504 black thin lines. In the context of future deepening and poleward migration of the ASL, stronger
505 southerly winds over the Ross Sea will lead to increased sea ice production on the Ross Sea
506 continental shelf. In the western Amundsen Sea, weakened easterly winds will reduce the
507 barotropic transport of ice shelf meltwater from the Amundsen Sea to the Ross Sea. In the
508 eastern Amundsen, weakened easterly winds will enhance CDW intrusion, promoting ice shelf
509 melting, and reducing the westward transport of meltwater. The ultimate effects of these
510 changes are enhancement in the DSW production and export in the Ross Sea.

511



512 *Data availability.* The model data that support the findings of this study are available at
513 <https://doi.org/10.5281/zenodo.18016271>. The ASL indices data are obtained from
514 https://scotthosking.com/asl_index.

515 *Author contributions.* ZZ formulated the original ideas presented in this manuscript. ZZ, HH
516 and CX conducted the model results analysis. ZZ and CX wrote the original manuscript draft.
517 HH, XW, YC, CW and CX contributed to the model development, and participated in the result
518 interpretation. All authors contributed to the article and approved the submitted version.

519 *Competing interests.* The contact author has declared that none of the authors has any
520 competing interests.

521 *Disclaimer.* Publisher's note: Copernicus Publications remains neutral with regard to
522 jurisdictional claims made in the text, published maps, institutional affiliations, or any other
523 geographical representation in this paper. While Copernicus Publications makes every effort
524 to include appropriate place names, the final responsibility lies with the authors.

525 *Acknowledgements.* This work is funded by the National Natural Science Foundation of China
526 (Grant No. 42476271), the Shanghai Pilot Program for Basic Research - Shanghai Jiao Tong
527 University (Grant No. 21TQ1400201), and the European Union's Horizon 2020 research and
528 innovation framework programme under Grant agreement no. 101003590 (PolarRES project).

529 *Financial support.* This research has been supported by the National Natural Science
530 Foundation of China (grant no. 42476271), the Shanghai Pilot Program for Basic Research of
531 Shanghai Jiao Tong University (grant no. 21TQ1400201), and the European Union's Horizon
532 2020 research and innovation framework programme under Grant agreement no. 101003590
533 (PolarRES project).



535

REFERENCES

- 536 Bretherton, C. S., Widmann, M., Dymnikov, V. P., Wallace, J. M., and Bladé, I.: The effective
537 number of spatial degrees of freedom of a time-varying field, *J. Clim.*, 12, 1990–2009,
538 [https://doi.org/10.1175/1520-0442\(1999\)012%3C1990:TENOSD%3E2.0.CO;2](https://doi.org/10.1175/1520-0442(1999)012%3C1990:TENOSD%3E2.0.CO;2), 1999.
- 539 Bromwich, D. H., and Kurtz, D. D.: Katabatic wind forcing of the Terra Nova Bay polynya, *J.*
540 *Geophys. Res.-Oceans*, 89, 3561–3572, <https://doi.org/10.1029/JC089iC03p03561>, 1984.
- 541 Bromwich, D. H., Nicolas, J. P., and Monaghan, A. J.: An Assessment of precipitation changes
542 over Antarctica and the Southern Ocean since 1989 in contemporary global reanalyses, *J.*
543 *Clim.*, 24, 4189–4209, <https://doi.org/10.1175/2011JCLI4074.1>, 2011.
- 544 Budgell, W. P.: Numerical simulation of ice-ocean variability in the Barents Sea region, *Ocean*
545 *Dyn.*, 55, 370–387, <https://doi.org/10.1007/s10236-005-0008-3>, 2005.
- 546 Castagno, P., Capozzi, V., DiTullio, G. R., Falco, P., Fusco, G., Rintoul, S. R., Spezie, G., and
547 Budillon, G.: Rebound of shelf water salinity in the Ross Sea, *Nat. Commun.*, 10, 1–6,
548 <https://doi.org/10.1038/s41467-019-12049-z>, 2019.
- 549 Chenoli, S. N., Turner, J., and Samah, A. A.: A strong wind event on the Ross Ice Shelf,
550 Antarctica: A case study of scale interactions, *Mon. Weather Rev.*, 143, 4163–4180,
551 <https://doi.org/10.1175/MWR-D-15-0002.1>, 2015.
- 552 Clem, K. R., Renwick, J. A., and McGregor, J.: Large-scale forcing of the Amundsen Sea Low
553 and its influence on sea ice and West Antarctic temperature, *J. Clim.*, 30, 8405–8424,
554 <https://doi.org/10.1175/JCLI-D-16-0891.1>, 2017.
- 555 Coggins, J. H. J., and McDonald, A. J.: The influence of the Amundsen Sea Low on the winds
556 in the Ross Sea and surroundings: Insights from a synoptic climatology, *J. Geophys. Res.*,
557 120, 2167–2189, <https://doi.org/10.1002/2014JD022830>, 2015.



- 558 Cohen, L., Dea, S., and Renwick, J.: Synoptic weather types for the Ross Sea region,
559 Antarctica, *J. Clim.*, 26, 636–649, <https://doi.org/10.1175/JCLI-D-11-00690.1>, 2013.
- 560 Dale, E. R., McDonald, A. J., Coggins, J. H. J., and Rack, W.: Atmospheric forcing of sea ice
561 anomalies in the Ross Sea polynya region, *The Cryosphere*, 11, 267–280,
562 <https://doi.org/10.5194/tc-11-267-2017>, 2017.
- 563 Depoorter, M. A., Bamber, J. L., Griggs, J. A., Lenaerts, J. T. M., Ligtenberg, S. R. M., Van
564 Den Broeke, M. R., and Moholdt, G.: Calving fluxes and basal melt rates of Antarctic ice
565 shelves, *Nature*, 502, 89–92, <https://doi.org/10.1038/nature12567>, 2013.
- 566 Dinniman, M. S., Klinck, J. M., and Smith, W. O.: A model study of Circumpolar Deep Water
567 on the West Antarctic Peninsula and Ross Sea continental shelves, *Deep-Sea Res. Part II*,
568 58, 1508–1523, <https://doi.org/10.1016/j.dsr2.2010.11.013>, 2011.
- 569 Dinniman, M. S., Klinck, J. M., Bai, L. S., Bromwich, D. H., Hines, K. M., and Holland, D.
570 M.: The effect of atmospheric forcing resolution on delivery of ocean heat to the Antarctic
571 floating ice shelves, *J. Clim.*, 28, 6067–6085, <https://doi.org/10.1175/JCLI-D-14-00374.1>,
572 2015.
- 573 Dinniman, M. S., Klinck, J. M., Hofmann, E. E., and Smith, W. O.: Effects of projected changes
574 in wind, atmospheric temperature, and freshwater inflow on the Ross Sea, *J. Clim.*, 31,
575 1619–1635, <https://doi.org/10.1175/JCLI-D-17-0351.1>, 2018.
- 576 Dotto, T. S., and coauthors: Variability of the Ross Gyre, Southern Ocean: Drivers and
577 Responses Revealed by Satellite Altimetry, *Geophys. Res. Lett.*, 45, 6195–6204,
578 <https://doi.org/10.1029/2018GL078607>, 2018.



- 579 Dotto, T. S., and coauthors: Control of the oceanic heat content of the Getz-Dotson Trough,
580 Antarctica, by the Amundsen Sea Low, *J. Geophys. Res.-Oceans*, 125, e2020JC016113,
581 <https://doi.org/10.1029/2020JC016113>, 2020.
- 582 Egbert, G. D., and Erofeeva, S. Y.: Efficient inverse modeling of barotropic ocean tides, *J.*
583 *Atmos. Ocean. Technol.*, 19, 183–204, [https://doi.org/10.1175/1520-0426\(2002\)019%3C0183:EIMOBO%3E2.0.CO;2](https://doi.org/10.1175/1520-0426(2002)019%3C0183:EIMOBO%3E2.0.CO;2), 2002.
- 585 Fusco, G., Budillon, G., and Spezie, G.: Surface heat fluxes and thermohaline variability in the
586 Ross Sea and in Terra Nova Bay polynya, *Cont. Shelf Res.*, 29, 1887–1895,
587 <https://doi.org/10.1016/j.csr.2009.07.006>, 2009.
- 588 Gao, M., Kim, S. J., Yang, J., Liu, J., Jiang, T., Su, B., Wang, Y., and Huang, J.: Historical
589 fidelity and future change of Amundsen Sea Low under 1.5 °C–4 °C global warming in
590 CMIP6, *Atmos. Res.*, 255, 105533, <https://doi.org/10.1016/j.atmosres.2021.105533>, 2021.
- 591 Guo, G., Gao, L., and Shi, J.: Modulation of dense shelf water salinity variability in the western
592 Ross Sea associated with the Amundsen Sea Low, *Environ. Res. Lett.*, 16, 014004,
593 <https://doi.org/10.1088/1748-9326/abc995>, 2021.
- 594 Haidvogel, D. B., and coauthors: Ocean forecasting in terrain-following coordinates:
595 Formulation and skill assessment of the Regional Ocean Modeling System, *J. Comput.*
596 *Phys.*, 227, 3595–3624, <https://doi.org/10.1016/j.jcp.2007.06.016>, 2008.
- 597 Häkkinen, S., and Mellor, G. L.: Modeling the seasonal variability of a coupled Arctic ice-
598 ocean system, *J. Geophys. Res.-Oceans*, 97, 20285–20304,
599 <https://doi.org/10.1029/92JC02037>, 1992.



- 600 Henley, B. J., Gergis, J., Karoly, D. J., Power, S., Kennedy, J., and Folland, C. K.: A Tripole
601 Index for the Interdecadal Pacific Oscillation, *Clim. Dyn.*, 45, 3077–3090,
602 <https://doi.org/10.1007/s00382-015-2525-1>, 2015.
- 603 Hersbach, H., and coauthors: The ERA5 global reanalysis, *Q. J. R. Meteorol. Soc.*, 146, 1999–
604 2049, <https://doi.org/10.1002/qj.3803>, 2020.
- 605 Holland, D. M., and Jenkins, A.: Modeling thermodynamic ice-ocean interactions at the base
606 of an ice shelf, *J. Phys. Oceanogr.*, 29, 1787–1800, [https://doi.org/10.1175/1520-0485\(1999\)029%3C1787:MTIOIA%3E2.0.CO;2](https://doi.org/10.1175/1520-0485(1999)029%3C1787:MTIOIA%3E2.0.CO;2), 1999.
- 608 Holland, M. M., Landrum, L., Raphael, M. N., and Kwok, R.: The Regional, Seasonal, and
609 Lagged Influence of the Amundsen Sea Low on Antarctic Sea Ice, *Geophys. Res. Lett.*, 45,
610 11227–11234, <https://doi.org/10.1029/2018GL080140>, 2018.
- 611 Hosking, J. S., Orr, A., Marshall, G. J., Turner, J., and Phillips, T.: The influence of the
612 Amundsen-Bellingshausen Seas Low on the climate of West Antarctica and its
613 representation in coupled climate model simulations, *J. Clim.*, 26, 6633–6648,
614 <https://doi.org/10.1175/JCLI-D-12-00813.1>, 2013.
- 615 Hosking, J. S., Orr, A., Bracegirdle, T. J., and Turner, J.: Future circulation changes off West
616 Antarctica: Sensitivity of the Amundsen Sea Low to projected anthropogenic forcing,
617 *Geophys. Res. Lett.*, 43, 367–376, <https://doi.org/10.1002/2015GL067143>, 2016.
- 618 Hunke, E. C.: Viscous-Plastic Sea Ice Dynamics with the EVP Model: Linearization Issues, *J.*
619 *Comput. Phys.*, 170, 18–38, <https://doi.org/10.1006/jcph.2001.6710>, 2001.
- 620 Hunke, E. C., and Dukowicz, J. K.: An elastic-viscous-plastic model for sea ice dynamics, *J.*
621 *Phys. Oceanogr.*, 27, 1849–1867, [https://doi.org/10.1175/1520-0485\(1997\)027%3C1849:AEVPMF%3E2.0.CO;2](https://doi.org/10.1175/1520-0485(1997)027%3C1849:AEVPMF%3E2.0.CO;2), 1997.



- 623 Jacobs, S., Giulivi, C., Dutrieux, P., Rignot, E., Nitsche, F., and Mouginot, J.: Getz Ice Shelf
624 melting response to changes in ocean forcing, *J. Geophys. Res.-Oceans*, 118, 4152–4168,
625 <https://doi.org/10.1002/jgrc.20298>, 2013.
- 626 Jacobs, S. S., and Giulivi, C. F.: Large multidecadal salinity trends near the Pacific-Antarctic
627 continental margin, *J. Clim.*, 23, 4508–4524, <https://doi.org/10.1175/2010JCLI3284.1>,
628 2010.
- 629 Jacobs, S. S., Giulivi, C. F., and Mele, P. A.: Freshening of the Ross Sea during the late 20th
630 century, *Science*, 297, 386–389, <https://doi.org/10.1126/science.1069574>, 2002.
- 631 Jacobs, S. S., Jenkins, A., Giulivi, C. F., and Dutrieux, P.: Stronger ocean circulation and
632 increased melting under Pine Island Glacier ice shelf, *Nat. Geosci.*, 4, 519–523,
633 <https://doi.org/10.1038/ngeo1188>, 2011.
- 634 Jacobs, S. S., Giulivi, C. F., and Dutrieux, P.: Persistent Ross Sea Freshening From Imbalance
635 West Antarctic Ice Shelf Melting, *J. Geophys. Res.-Oceans*, 127, e2021JC017808,
636 <https://doi.org/10.1029/2021JC017808>, 2022.
- 637 Jendersie, S., Williams, M. J. M., Langhorne, P. J., and Robertson, R.: The Density-Driven
638 Winter Intensification of the Ross Sea Circulation, *J. Geophys. Res.-Oceans*, 123, 7702–
639 7724, <https://doi.org/10.1029/2018JC013965>, 2018.
- 640 Jenkins, A., Shoosmith, D., Dutrieux, P., Jacobs, S., Kim, T. W., Lee, S. H., Ha, H. K., and
641 Stammerjohn, S.: West Antarctic Ice Sheet retreat in the Amundsen Sea driven by decadal
642 oceanic variability, *Nat. Geosci.*, 11, 733–738, <https://doi.org/10.1038/s41561-018-0207-4>, 2018.



- 644 Kim, C. S., Kim, T. W., Cho, K. H., Ha, H. K., Lee, S. H., Kim, H. C., and Lee, J. H.: Variability
645 of the Antarctic Coastal Current in the Amundsen Sea, *Estuar. Coast. Shelf Sci.*, 181, 123–
646 133, <https://doi.org/10.1016/j.ecss.2016.08.004>, 2016.
- 647 Konrad, H., Shepherd, A., Gilbert, L., Hogg, A. E., McMillan, M., Muir, A., and Slater, T.: Net
648 retreat of Antarctic glacier grounding lines, *Nat. Geosci.*, 11, 258–262,
649 <https://doi.org/10.1038/s41561-018-0082-z>, 2018.
- 650 Kusahara, K., Williams, G. D., Tamura, T., Massom, R., and Hasumi, H.: Dense shelf water
651 spreading from Antarctic coastal polynyas to the deep Southern Ocean: A regional
652 circumpolar model study, *J. Geophys. Res.-Oceans*, 122, 6238–6253,
653 <https://doi.org/10.1002/2017JC012911>, 2017.
- 654 Large, W. G., McWilliams, J. C., and Doney, S. C.: Oceanic vertical mixing: A review and a
655 model with a nonlocal boundary layer parameterization, *Rev. Geophys.*, 32, 363–403,
656 <https://doi.org/10.1029/94RG01872>, 1994.
- 657 De Lavergne, C., Madec, G., Roquet, F., Holmes, R. M., and McDougall, T. J.: Abyssal ocean
658 overturning shaped by seafloor distribution, *Nature*, 551, 181–186,
659 <https://doi.org/10.1038/nature24472>, 2017.
- 660 Li, Z., Wang, C., and Zhou, M.: A model analysis of circumpolar deep water intrusions on the
661 continental shelf break in Amundsen Sea, Antarctica, *J. Geophys. Res.-Oceans*, 130,
662 e2024JC022210, <https://doi.org/10.1029/2024JC022210>, 2025.
- 663 Li, X., Cai, W., Meehl, G., Chen, D., Yuan, X., Raphael, M., Holland, D., Ding, Q., Fogt, R.,
664 Markle, B., Wang, G., Bromwich, D., Turner, J., Xie, S.-P., Steig, E., Gille, S., Xiao, C.,
665 Wu, B., Lazzara, M., and Song, C.: Tropical teleconnection impacts on Antarctic climate
666 changes, *Nat. Rev. Earth Environ.*, 2, 680–698, <https://doi.org/10.1038/s43017-021-00204-5>, 2021.



- 668 MacLachlan, C., Arribas, A., Peterson, K. A., Maidens, A., Fereday, D., Scaife, A. A., Gordon,
669 M., Vellinga, M., Williams, A., Comer, R. E., Camp, J., Xavier, P., and Madec, G.: Global
670 Seasonal Forecast System version 5 (GloSea5): A high-resolution seasonal forecast system,
671 *Q. J. R. Meteorol. Soc.*, 141, 1072–1084, <https://doi.org/10.1002/qj.2396>, 2015.
- 672 Marshall, J., and Speer, K.: Closure of the meridional overturning circulation through Southern
673 Ocean upwelling, *Nat. Geosci.*, 5, 171–180, <https://doi.org/10.1038/ngeo1391>, 2012.
- 674 Mellor, G. L., and Kantha, L.: An ice-ocean coupled model, *J. Geophys. Res.*, 94, 10937–
675 10954, <https://doi.org/10.1029/JC094iC08p10937>, 1989.
- 676 Morlighem, M., Rignot, E., Mouginot, J., Seroussi, H., Bamber, J. N., Aschwanden, A. A.,
677 Bartholomaus, T. A., Bindschadler, R., Bjørk, G., Brunt, K. M., Chinn, D. N., Paden, J. D.,
678 Fricker, H. A., Jezek, K., Joughin, I., Khan, A., Krabill, W. B., Larsen, A. P., Li, J., Klenger,
679 C. M., Marder, S. R., Millan, B. M., Porter, D. J., Routhier, M. J., Schlegel, M., Smith, B.,
680 Wang, J. Y., Willis, J. J., Williams, G. D., and Winter, J. G.: Deep glacial troughs and
681 stabilizing ridges unveiled beneath the margins of the Antarctic ice sheet, *Nat. Geosci.*, 13,
682 132–137, <https://doi.org/10.1038/s41561-019-0510-8>, 2020.
- 683 Nakata, K., Ohshima, K. I., and Nihashi, S.: Mapping of Active Frazil for Antarctic Coastal
684 Polynyas, With an Estimation of Sea-Ice Production, *Geophys. Res. Lett.*, 48,
685 e2020GL091353, <https://doi.org/10.1029/2020GL091353>, 2021.
- 686 Nakayama, Y., Schröder, M., and Hellmer, H. H.: From circumpolar deep water to the glacial
687 meltwater plume on the eastern Amundsen Shelf, *Deep-Sea Res. Part I*, 77, 50–62,
688 <https://doi.org/10.1016/j.dsr.2013.04.001>, 2013.
- 689 Nakayama, Y., Timmermann, R., Rodehacke, C. B., Schröder, M., and Hellmer, H. H.:
690 Modeling the spreading of glacial meltwater from the Amundsen and Bellingshausen Seas,
691 *Geophys. Res. Lett.*, 41, 7942–7949, <https://doi.org/10.1002/2014GL061600>, 2014.



- 692 Naughten, K. A., Meissner, K. J., Galton-Fenzi, B. K., England, M. H., Timmermann, R.,
693 Hellmer, H. H., Hattermann, T., and Debernard, J. B.: Intercomparison of Antarctic ice-
694 shelf, ocean, and sea-ice interactions simulated by MetROMS-iceshelf and FESOM 1.4,
695 Geosci. Model Dev., 11, 1257–1292, <https://doi.org/10.5194/gmd-11-1257-2018>, 2018.
- 696 Nicolas, J. P., and Bromwich, D. H.: Climate of West Antarctica and influence of marine air
697 intrusions, J. Clim., 24, 49–67, <https://doi.org/10.1175/2010JCLI3522.1>, 2011.
- 698 Nihashi, S., and Ohshima, K. I.: Circumpolar mapping of Antarctic coastal polynyas and
699 landfast sea ice: Relationship and variability, J. Clim., 28, 3650–3670,
700 <https://doi.org/10.1175/JCLI-D-14-00369.1>, 2015.
- 701 Núñez-Riboni, I., and Fahrbach, E.: Seasonal variability of the Antarctic Coastal Current and
702 its driving mechanisms in the Weddell Sea, Deep-Sea Res. Part I, 56, 1927–1941,
703 <https://doi.org/10.1016/j.dsr.2009.06.005>, 2009.
- 704 Orsi, A. H., and Wiederwohl, C. L.: A recount of Ross Sea waters, Deep-Sea Res. Part II, 56,
705 778–795, <https://doi.org/10.1016/j.dsr2.2008.10.033>, 2009.
- 706 Paolo, F. S., Fricker, H. A., and Padman, L.: Volume loss from Antarctic ice shelves is
707 accelerating, Science, 348, 327–331, <https://doi.org/10.1126/science.aaa0940>, 2015.
- 708 Park, J., Kim, H. C., Jo, Y. H., Kidwell, A., and Hwang, J.: Multi-temporal variation of the
709 Ross Sea Polynya in response to climate forcings, Polar Res., 37, 1444891,
710 <https://doi.org/10.1080/17518369.2018.1444891>, 2018.
- 711 Raphael, M. N., and coauthors: The Amundsen sea low: Variability, change, and impact on
712 Antarctic climate, Bull. Am. Meteorol. Soc., 97, 111–121, <https://doi.org/10.1175/BAMS-D-14-00018.1>, 2016.



- 714 Raphael, M. N., Holland, M. M., Landrum, L., and Hobbs, W. R.: Links between the Amundsen
715 Sea Low and sea ice in the Ross Sea: seasonal and interannual relationships, *Clim. Dyn.*,
716 52, 2333–2349, <https://doi.org/10.1007/s00382-018-4258-4>, 2019.
- 717 Rignot, E., Jacobs, S., Mouginot, J., and Scheuchl, B.: Ice-shelf melting around Antarctica,
718 *Science*, 341, 266–270, <https://doi.org/10.1126/science.1235798>, 2013.
- 719 Rignot, E., Mouginot, J., Scheuchl, B., Van Den Broeke, M., Van Wessem, M. J., and
720 Morlighem, M.: Four decades of Antarctic ice sheet mass balance from 1979–2017, *Proc.*
721 *Natl. Acad. Sci. U. S. A.*, 116, 1095–1103, <https://doi.org/10.1073/pnas.1812883116>, 2019.
- 722 Rintoul, S. R.: Rapid freshening of Antarctic Bottom Water formed in the Indian and Pacific
723 oceans, *Geophys. Res. Lett.*, 34, L06606, <https://doi.org/10.1029/2006GL028550>, 2007.
- 724 Shchepetkin, A. F., and McWilliams, J. C.: Correction and commentary for “Ocean forecasting
725 in terrain-following coordinates: Formulation and skill assessment of the Regional Ocean
726 Modeling System” by Haidvogel et al., *J. Comput. Phys.*, 228, 8985–9000,
727 <https://doi.org/10.1016/j.jcp.2009.09.002>, 2009.
- 728 Shepherd, A., Ivins, E., Rignot, E., Smith, B., van den Broeke, M., and Velicogna, I.: Mass
729 balance of the Antarctic Ice Sheet from 1992 to 2017, *Nature*, 558, 219–222,
730 <https://doi.org/10.1038/s41586-018-0179-y>, 2018.
- 731 Sigman, D. M., and Boyle, E. A.: Glacial/interglacial variations in atmospheric carbon dioxide,
732 *Nature*, 407, 859–869, <https://doi.org/10.1038/35038000>, 2000.
- 733 Silvano, A., Rintoul, S. R., Peña-Molino, B., Hobbs, W. R., van Wijk, E., Aoki, S., Tamura,
734 T., and Williams, G. D.: Freshening by glacial meltwater enhances melting of ice shelves
735 and reduces formation of Antarctic Bottom Water, *Sci. Adv.*, 4, eaap9467,
736 <https://doi.org/10.1126/sciadv.aap9467>, 2018.



- 737 Silvano, A., and coauthors: Recent recovery of Antarctic Bottom Water formation in the Ross
738 Sea driven by climate anomalies, *Nat. Geosci.*, 13, 780–786,
739 <https://doi.org/10.1038/s41561-020-00655-3>, 2020.
- 740 Silvano, A., and coauthors: Baroclinic Ocean Response to Climate Forcing Regulates Decadal
741 Variability of Ice-Shelf Melting in the Amundsen Sea, *Geophys. Res. Lett.*, 49,
742 e2022GL100646, <https://doi.org/10.1029/2022GL100646>, 2022.
- 743 Spreen, G., Kaleschke, L., and Heygster, G.: Sea ice remote sensing using AMSR-E 89-GHz
744 channels, *J. Geophys. Res.*, 113, C02S03, <https://doi.org/10.1029/2005JC003384>, 2008.
- 745 Tamura, T., Ohshima, K. I., Fraser, A. D., and Williams, G. D.: Sea ice production variability
746 in Antarctic coastal polynyas, *J. Geophys. Res.-Oceans*, 121, 2967–2979,
747 <https://doi.org/10.1002/2015JC011537>, 2016.
- 748 Tewari, K., Mishra, S. K., Salunke, P., and Dewan, A.: Future projections of temperature and
749 precipitation for Antarctica, *Environ. Res. Lett.*, 17, 014029, <https://doi.org/10.1088/1748-9326/ac43e2>, 2022.
- 750 Thoma, M., Jenkins, A., Holland, D., and Jacobs, S.: Modelling Circumpolar Deep Water
751 intrusions on the Amundsen Sea continental shelf, Antarctica, *Geophys. Res. Lett.*, 35, 2–
752 7, <https://doi.org/10.1029/2008GL034939>, 2008.
- 753 Treasure, A. M., and coauthors: Marine Mammals Exploring the Oceans Pole to Pole: A
754 Review of the MEOP Consortium, *Oceanography*, 30, 132–138,
755 <https://doi.org/10.5670/oceanog.2017.234>, 2017.
- 756 Turner, J., Phillips, T., Hosking, J. S., Marshall, G. J., and Orr, A.: The Amundsen Sea Low,
757 *Int. J. Climatol.*, 33, 1818–1829, <https://doi.org/10.1002/joc.3558>, 2013.



- 759 Xie, C., Zhang, Z., Chen, Y., and Wang, C.: Substantial contraction of dense shelf water in the
760 Ross Sea under future climate scenarios, *Geophys. Res. Lett.*, 52, e2024GL112581,
761 <https://doi.org/10.1029/2024GL112581>, 2025.
- 762 Xie, C., Zhang, Z., Chen, Y., Wang, C., and Zhou, M.: The response of Ross Sea shelf water
763 properties to enhanced Amundsen Sea ice shelf melting, *J. Geophys. Res.-Oceans*, 129,
764 e2024JC020919, <https://doi.org/10.1029/2024JC020919>, 2024.
- 765 Wåhlin, A. K., and coauthors: Variability of warm deep water inflow in a submarine trough on
766 the Amundsen Sea shelf, *J. Phys. Oceanogr.*, 43, 2054 – 2070, <https://doi.org/10.1175/JPO-D-12-0157.1>, 2013.
- 768 Wang, S., Liu, J., Cheng, X., Yang, D., Kerzenmacher, T., Li, X., Hu, Y., and Braesicke, P.:
769 Contribution of the deepened Amundsen sea low to the record low Antarctic sea ice extent
770 in February 2022, *Environ. Res. Lett.*, 18, 054002, <https://doi.org/10.1088/1748-9326/acc9d6>, 2023.
- 772 Wang, T., Wei, H., and Xiao, J.: Dynamic linkage between the interannual variability of the
773 spring Ross Ice Shelf Polynya and the atmospheric circulation anomalies, *Clim. Dyn.*, 53,
774 831 – 840, <https://doi.org/10.1007/s00382-021-05936-0>, 2022.
- 775 Wang, X., Zhang, Z., Wang, X., Vihma, T., Zhou, M., Yu, L., Uotila, P., and Sein, D. V.:
776 Impacts of strong wind events on sea ice and water mass properties in Antarctic coastal
777 polynyas, *Clim. Dyn.*, 57, 3505 – 3528, <https://doi.org/10.1007/s00382-021-05878-7>,
778 2021.
- 779 Wang, X., Zhang, Z., Dinniman, M. S., Uotila, P., Li, X., and Zhou, M.: The response of sea
780 ice and high-salinity shelf water in the Ross Ice Shelf Polynya to cyclonic atmosphere



- 781 circulations, *The Cryosphere*, 17, 1107–1126, <https://doi.org/10.5194/tc-17-1107-2023>,
782 2023.
- 783 Weber, N. J., Lazzara, M. A., Keller, L. M., and Cassano, J. J.: The extreme wind events in the
784 Ross Island region of Antarctica, *Weather Forecast.*, 31, 985 – 1000,
785 <https://doi.org/10.1175/WAF-D-15-0125.1>, 2016.
- 786 van Wijk, E. M., and Rintoul, S. R.: Freshening drives contraction of Antarctic Bottom Water
787 in the Australian Antarctic Basin, *Geophys. Res. Lett.*, 41, 1657–1664,
788 <https://doi.org/10.1002/2013GL058921>, 2014.
- 789 Zhang, X., Hetland, R. D., Marta-Almeida, M., and Dimarco, S. F.: A numerical investigation
790 of the Mississippi and Atchafalaya freshwater transport, filling and flushing times on the
791 Texas-Louisiana Shelf, *J. Geophys. Res.-Oceans*, 117, 1–21,
792 <https://doi.org/10.1029/2012JC00810>, 2012.
- 793 Zhang, Z., Xie, C., Castagno, P., England, M. H., Wang, X., Dinniman, M. S., Silvano, A.,
794 Wang, C., Zhou, L., Li, X., Zhou, M., and Budillon, G.: Evidence for large-scale climate
795 forcing of dense shelf water variability in the Ross Sea, *Nat. Commun.*, 15, 8190,
796 <https://doi.org/10.1038/s41467-024-52524-x>, 2024.
- 797 Zhang, Z., Xie, C., Wang, C., Chen, Y., Hu, H., and Wang, X.: The Ross Sea and Amundsen
798 Sea Ice–Sea Model (RAISE v1.0): A high-resolution ocean–sea ice–ice shelf coupling
799 model for simulating the dense shelf water and Antarctic Bottom Water in the Ross Sea,
800 Antarctica, *Geosci. Model Dev.*, 18, 1375–1393, <https://doi.org/10.5194/gmd-18-1375-2025>, 2025.



802 Zhang, Z., Vihma, T., Stössel, A., and Uotila, P.: The role of wind forcing from operational
803 analyses for the model representation of Antarctic coastal sea ice, *Ocean Model.*, 94, 95 -
804 111 <http://dx.doi.org/10.1016/j.ocemod.2015.07.019>, 2015.
805
806